Cobalt (Oxy)hydroxide Nanosheets Supported on Nickel Foam as Efficient Electrocatalysts for Oxygen Evolution

Zackary S. Parsons, ¹ Lorianne R. Shultz-Johnson, ² Titel Jurca, ^{2,3,4*} and Xiaofeng Feng ^{1,2,3,4,5*}

ABSTRACT:

Oxygen evolution reaction (OER) plays an essential role as the anodic reaction in numerous electrochemical systems for renewable energy conversion. However, the design of efficient electrocatalysts for the OER has been impeded by the sluggish kinetics and poor stability of the catalyst materials. Fe, Co, and Ni-based oxides and (oxy)hydroxides exhibit high OER activities, while the active phases of these catalysts are yet to be elucidated. Here we report a facile synthesis of Co (oxy)hydroxide and oxide nanosheets supported on Ni foam as OER electrocatalysts. An Ni foam support was submerged into a CoCl₂ solution and heated to evenly coat the support with Co species, which was converted to Co (oxy)hydroxides or oxides by further annealing at various temperatures. The prepared electrodes showed high active surface areas and high OER activities, which depended on the annealing temperature that impacted the structure and chemical state of the Co species. The electrode annealed at a lower temperature showed a higher intrinsic activity for the OER, commensurate with the presence of Co (oxy)hydroxide phases that are most active for the OER. Our work sheds new insights into the structure-activity relationships of Co-based OER electrocatalysts for efficient electrolyzers.

KEYWORDS: Electrocatalysis, oxygen evolution reaction (OER), Co oxyhydroxide, Co oxide, intrinsic activity, active phase

¹Department of Physics, University of Central Florida, Orlando, Florida 32816, United States

²Department of Chemistry, University of Central Florida, Orlando, Florida 32816, United States

³Renewable Energy and Chemical Transformations (REACT) Cluster, University of Central Florida, Orlando, Florida 32816, United States

⁴NanoScience and Technology Center (NSTC), University of Central Florida, Orlando, Florida, 32826, United States

⁵Department of Materials Science and Engineering, University of Central Florida, Orlando, Florida 32816, United States

^{*}Email: <u>Titel.Jurca@ucf.edu</u> (T.J.); <u>Xiaofeng.Feng@ucf.edu</u> (X.F.)

INTRODUCTION

Due to the limited reserves of fossil fuels and the increasing environmental concerns, there is an urgent need for renewable energy technologies that can efficiently convert and utilize solar and wind energy. Considering the intermittency of solar and wind resources, it is desirable to convert and store solar- and wind-generated electricity into chemical energy. One promising approach is to use the renewable electricity to power the electrosynthesis of chemicals and fuels from naturally abundant resources. For example, renewably powered electrochemical water splitting can provide a sustainable route for the production of H_2 as a clean, carbon-free fuel. Substantial efforts have also been made to develop electrolyzers for the conversion of CO_2 to value-added chemicals such as ethylene and ethanol, as well as many other electrochemical processes. In the electrolyzers, the reaction occurring on the anode is typically the oxygen evolution reaction (OER): $4OH^- \rightarrow O_2 + 2H_2O + 4e^-$, which has sluggish kinetics. Therefore, developing efficient electrocatalysts for the OER is essential to lower the anodic overpotential and thus improve the overall performance and energy efficiency of the electrolyzers.

The design of efficient OER electrocatalysts has been impeded by the sluggish kinetics and poor stability of the catalyst materials under anodic oxidation conditions.^{5–9} To date, a variety of materials have been explored as electrocatalysts for the OER, including precious metal oxides, ^{10–12} non-precious metal oxides, ^{13–16} and non-oxide compounds. ^{17–20} Precious metal oxides, particularly RuO_x and IrO_x, show high OER activities and can sustain at high anodic potentials in both acidic and alkaline electrolytes, ^{10–12} but the high cost of precious metals limits their practical applications. Meanwhile, non-precious metal oxides, particularly Fe, Co, Ni-based oxides or (oxy)hydroxides, have shown remarkable activities for the OER, ^{13,14} and their low cost and high stability in alkaline solutions make them promising OER catalysts. These materials have multiple oxidation states and coordination environments, and thus allow different combinations of transition metals to form bimetallic or multi-metallic oxides, 15,16 resulting in a widely tunable structural and chemical space. In addition, non-oxide compounds such as metal chalcogenides and pnictides as well as carbonbased materials have been reported as promising catalysts for both hydrogen evolution reaction (HER) and OER, ^{17–20} so they may be suitable candidates for overall water splitting. Compared to transition metal oxides, only a limited number of non-oxide catalyst materials have been reported, and these materials still suffer from the need of high overpotentials for the OER.

Among the candidate materials, Co-based electrocatalysts have attracted substantial interest for the OER,^{21–39} as they allow for the formation of multi-cobalt centers with multiple/variable Co oxidation states (namely II, III, and IV).²¹ Accordingly, different phases of Co oxide, hydroxide, and oxyhydroxide, particularly Co₃O₄, Co(OH)₂, and CoOOH, have been studied for the OER.^{21–34} For example, Haase et al. uncovered the size-dependent activity and active oxidation state of Co oxide nanoparticles during the OER.²⁶ Gu et al. reported that Co(OH)₂ supported on Ni foam will

be electrochemically oxidized to Co₃O₄ during the OER.²⁷ Using correlative operando microscopy, Mefford et al. confirmed that CoOOH is the active site or reactant state of the rate-limiting step for the OER,³¹ while Moysiadou et al. found the dominating resting state of the catalyst under OER conditions to be the Co(IV) species CoO₂.³² Additionally, the redox properties and local bonding environment of Co₃O₄ can be modified by introducing CeO₂,³⁵ which allows Co(III) species to be easily oxidized into catalytically active Co(IV) species and thus enhances its intrinsic activity for the OER. While these works contributed substantially to the understandings of Co-based catalysts for the OER, further efforts are still needed to elucidate such a complicated system.

In this work, we developed Co (oxy)hydroxide and oxide nanosheets supported on Ni foam as electrocatalysts for the OER. The Co-based electrocatalysts were prepared by submerging a Ni foam support into a CoCl₂ solution and then heating to coat the support with Co species, followed by annealing to different temperatures to convert the Co species to (oxy)hydroxides or oxides. The prepared CoO_x/Ni-foam samples have systematically tuned morphologies and Co oxidation states, thus allowing a comparison to reveal the effect of Co oxidation states on the OER. As a result, we found that the electrode prepared with a lower annealing temperature (150 °C) exhibited a higher intrinsic activity for the OER than other electrodes prepared at higher temperatures, which was attributed to a higher prevalence of the Co (oxy)hydroxide phases in the sample. Our work provides new insights into the structure-activity relationships of Co-based OER electrocatalysts towards a rational design of OER catalysts.

EXPERIMENTAL SECTION

Materials Synthesis. A schematic illustration of the synthesis process of Ni-foam-supported Co oxide samples is shown in Figure 1a. First, 210 mg of cobalt chloride hexahydrate and 210 mg of Ni foam were added into deionized water so that they were fully immersed with a total solution volume of ~500 mL. The solution was then put into a sealed heavy-walled glass vessel to facilitate hydrothermal synthesis under elevated temperature and pressure. The solution was kept at 100 °C for 24 h while being stirred, and the color of the solution changed from a purple/pink to a dull grey/brown color during the process. Subsequently, the Ni foam was taken out from the flask and rinsed with copious amounts of deionized water, and then dried under ambient conditions overnight. The samples were then heated at 150 °C for 6 h in a muffle furnace under ambient atmosphere, and the resulting samples are hereafter referred to as CoO_x/Ni-Foam-150C samples. Some of the samples were put back into the furnace and further heated to different temperatures (350, 500, or 650 °C) at a ramp rate of 5 K min⁻¹ and held at each indicated temperature for 2 h. The derived samples are hereafter referred to as CoO_x/Ni-Foam-500C, and CoO_x/Ni-Foam-650C, respectively.

Materials Characterization. Scanning electron microscopy (SEM) images and energy dispersive spectroscopy (EDS) mapping were acquired using a ZEISS Ultra-55 FEG scanning electron microscope equipped with a Noran System 7 EDS with Silicon Drift Detector. X-ray photoelectron spectra (XPS) were acquired using a Thermo Scientific ESCALAB XI⁺ X-ray Photoelectron Spectrometer with an Al Kα X-ray source (1486.67 eV). Fourier transform infrared (FTIR) spectra were acquired using a JASCO FTIR-6600 Spectrometer equipped with a diamond attenuated total reflection (ATR) accessory in the range of 400–4000 cm⁻¹ with a resolution of 4 cm⁻¹.

Electrochemical Measurements. Electrochemical measurements were carried out using a CH Instruments 760E Bipotentiostat or a Gamry Interface 1000B Potentiostat. The above prepared CoO_x/Ni-Foam electrodes with a geometric area of 1 cm × 1 cm were used as the working electrodes, and a piece of Pt gauze (1 cm × 3 cm) and an Hg/HgO electrode (1 M KOH) were used as the counter electrode and the reference electrode, respectively. Linear sweep voltammetry (LSV) measurements were performed with 1 M KOH electrolyte in a single-compartment cell, where the working and counter electrodes were placed parallel to each other about 0.5 cm apart. O₂ gas was bubbled into the electrolyte at 5 sccm for at least 15 min prior to LSV scans but was stopped during the scans. Bulk electrolysis was performed using a two-compartment electrochemical cell (H-cell) separated by a piece of Nafion 1110 membrane at room temperature, as shown in Figure S1. During bulk electrolysis, O₂ gas was bubbled into the 1 M KOH electrolyte at a flow rate of 5 sccm with the electrolyte being stirred at 600 rpm. All potentials were iR-compensated and converted to the reversible hydrogen electrode (RHE) scale in this work. Electrochemical impedance spectroscopy (EIS) tests were performed in the frequency window ranging from 1 to 10^6 Hz with an amplitude of 5 mV. The electrochemical surface area (ECSA) of an electrode was quantified by measuring the double-layer capacitance. Cyclic voltammetry (CV) scans were performed on an electrode at different scan rates in a potential window of 0.8-0.9 V vs RHE, where only double-layer charging and discharging occur (no Faradaic process). The double-layer charging current was plotted vs the CV scan rate, and the slope of the linear regression gave the double-layer capacitance.

RESULTS AND DISCUSSION

A series of Co oxide samples supported on Ni foam were prepared using the method described in the Experimental Section (Figure 1a). The samples were prepared through thermal treatment at different temperatures ranging from 150 to 650 °C to tune their morphology and oxidation state for comparative structure-activity relationship studies. The samples were first characterized using SEM to reveal their morphology. Typical SEM images of the four electrodes are shown in Figure 1b–e, with corresponding overview SEM images exhibited in Figure S2. The CoO_x/Ni-Foam-150C sample consists of hexagonal nanosheets of around 1 µm in size (Figure 1b), which are most likely Co(OH)₂ or CoOOH nanosheets based on the expected morphology from prior studies.^{27,31,40}

To check the distribution of Co species on the Ni foam support, EDS mapping was performed on the sample, which confirmed a uniform distribution of Co, Ni, and O elements (Figure S3).

Annealing of the sample to higher temperature in air is expected to lead to the formation of Co oxides due to the decomposition of Co (oxy)hydroxides and further oxidation of Co. 40 Indeed, after annealing at 350 °C, most of the hexagonal nanosheets disappeared, which likely merged to form larger and more continues micro/nanostructured films (Figure 1c). This trend of morphology change continued in the sample after annealing at 500 °C (Figure 1d), until smaller nanoparticles were formed in the sample after annealing at 650 °C (Figure 1e). Basically, along with the increase of the annealing temperature, the morphology of the Co-based samples changed from hexagonal nanosheets to thin films, and eventually nanoparticles. Similarly, EDS mapping also confirmed a uniform distribution of Co, Ni, and O elements on the three samples (Figure S4–S6).

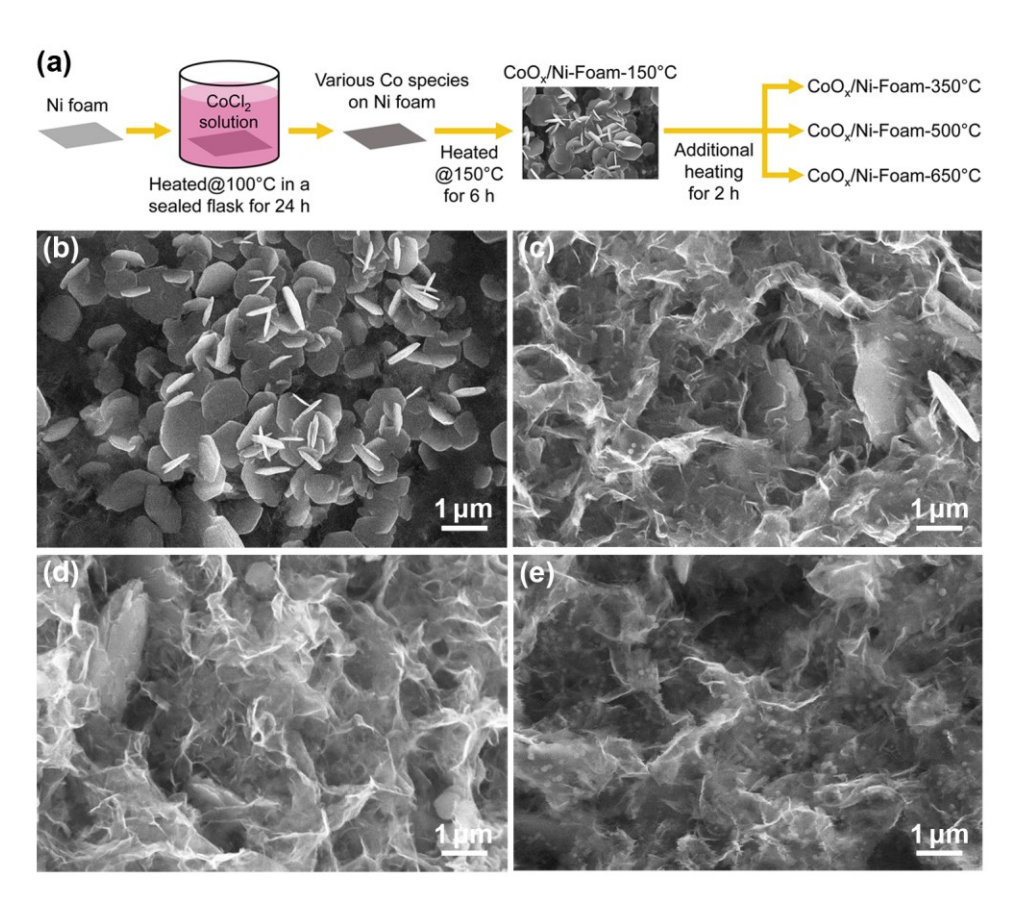


Figure 1. Synthesis and SEM characterization of the Co oxide samples supported on Ni foam. (a) Schematic illustration showing the procedure for the preparation of different Co-based samples. (b–e) Typical SEM images of the as-prepared samples: (b) CoO_x/Ni-Foam-150C; (c) CoO_x/Ni-Foam-350C; (d) CoO_x/Ni-Foam-500C; (e) CoO_x/Ni-Foam-650C.

XPS spectra were then acquired to examine the oxidation states of Co in the samples. Figure 2 shows high-resolution XPS spectra of the Co 2p region in the four samples, with corresponding spectra of the O 1s region presented in Figure S7. Deconvolution of the Co 2p_{3/2} region of the CoO_x/Ni-Foam-150C sample gave multiple peaks: a peak centered at ~780.2 eV that is attributed to CoOOH or $\mathrm{Co^{3+}}$ species, $\mathrm{^{40-42}}$ another peak centered at ~ 781.8 eV that is attributed to $\mathrm{Co(OH)_2}$ or Co²⁺, as well as two satellite peaks, as labelled in Figure 2a. Accordingly, the O 1s region of the sample in Figure S7(a) shows two peaks centered at 530.0 and 531.5 eV, which are assigned to O species in CoOOH and Co(OH)₂, respectively. 40-42 Based on the deconvoluted peak areas, the ratio of Co³⁺ species in the CoO_x/Ni-Foam-150C sample was estimated to be 73.7%, with the remaining 26.3% as Co²⁺. The XPS spectra of the rest three samples were similarly analyzed, as presented in Figure 2b-d and Figure S7(b-d), with similar peak positions. The ratio of Co³⁺ species decreased to ~68% in the CoO_x/Ni-Foam-350C and CoO_x/Ni-Foam-500C samples, but increased slightly to 70.7% in the CoO_x/Ni-Foam-650C sample. Therefore, as the annealing temperature of the samples increased from 150 to 500 °C, the ratio of Co³⁺ species decreased, due to the decomposition of Co (oxy)hydroxides and the formation of Co oxides, or namely surface and bulk CoOOH converts to predominantly Co₃O₄ (2:1 Co³⁺:Co²⁺) with increasing temperature.⁴⁰ Annealing to further higher temperature (650 °C) caused further oxidation to increase the ratio of Co³⁺ species in the Co oxides. A summary of the ratio of Co³⁺ and Co²⁺ species in the samples is presented in Table 1.

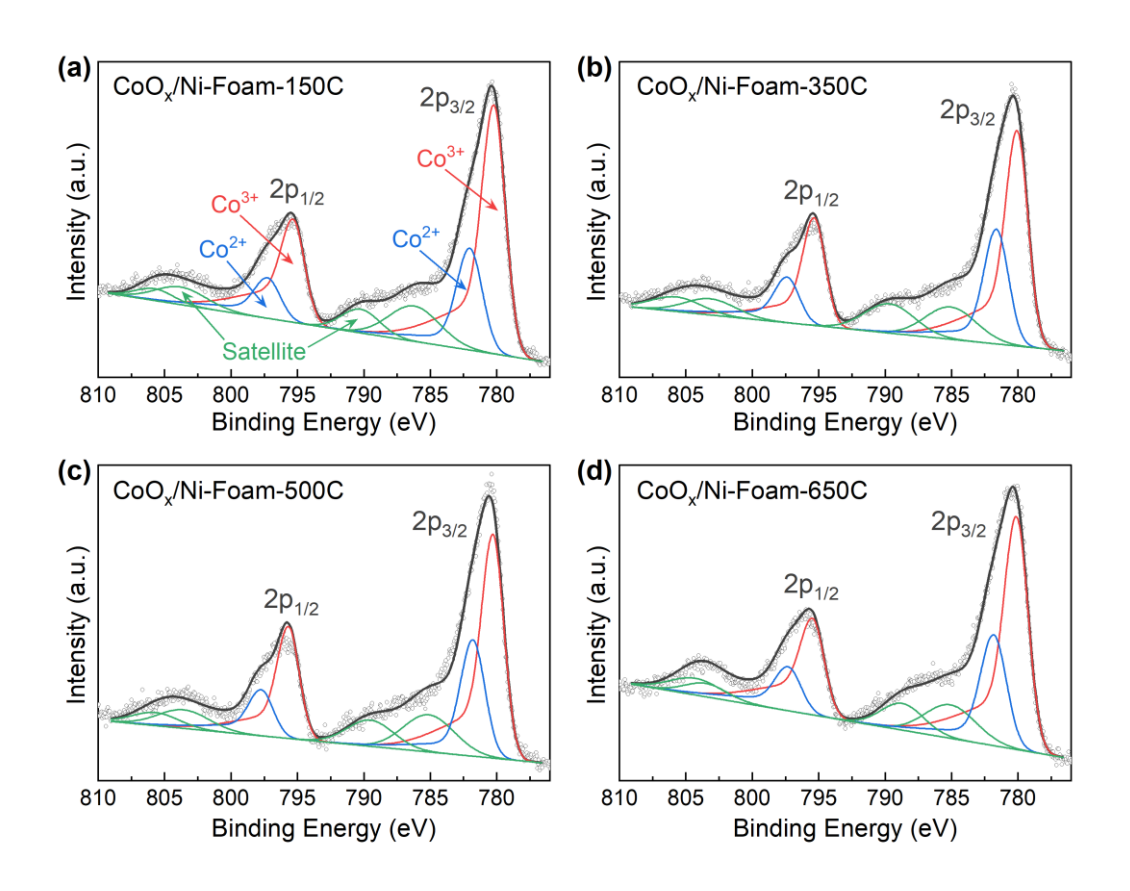


Figure 2. XPS spectra of the Co 2p region of the as-prepared samples, with deconvoluted peaks showing different oxidation states of Co: (a) CoO_x/Ni-Foam-150C; (b) CoO_x/Ni-Foam-350C; (c) CoO_x/Ni-Foam-500C; (d) CoO_x/Ni-Foam-650C.

Table 1. Summary of the Co oxidation states in the electrodes, as derived from the XPS data.

Sample	As-Prepared		After 2-h OER Test	
	Co ³⁺ Ratio	Co ²⁺ Ratio	Co ³⁺ Ratio	Co ²⁺ Ratio
CoO _x /Ni-Foam-150C	73.7%	26.3%	79.7%	20.3%
CoO _x /Ni-Foam-350C	68.2%	31.8%	75.8%	24.2%
CoO _x /Ni-Foam-500C	68.7%	31.3%	69.8%	30.2%
CoO _x /Ni-Foam-650C	70.7%	29.3%	75.6%	24.4%

To further reveal the chemical states and phases of Co species in the samples, FTIR spectra were acquired using a JASCO FTIR-6600 Spectrometer equipped with a diamond ATR accessory in the range of 400–4000 cm⁻¹ with a 4 cm⁻¹ resolution, as shown in Figure 3. Bare Ni foam shows no significant spectral features. The CoO_x/Ni-Foam-150C sample shows weak signals at 562 and 654 cm⁻¹, which are the characteristics of Co-O vibrations of spinel Co oxide. 43-45 The peak at 562 cm⁻¹ also appears to be broader than anticipated, and potentially multi-modal due to a secondary component. In addition, a very broad O-H stretching is observed at 3390 cm⁻¹, along with several other signals at 1357 and 1004 cm⁻¹, which are commensurate with the presence of water and surface hydroxides. 43-45 These observations are consistent with a mixture of CoOOH, Co(OH)2, and CoO_x. Given the low annealing temperature and storage in ambient air, it is anticipated that such a mixture would arise. Samples annealed at higher temperatures in air give rise to sharper, higher intensity signals at ca. 552 and 652 cm⁻¹, along with a marked disappearance of the very broad peak at 3390 cm⁻¹. This is consistent with the decomposition of Co (oxy)hydroxides and the formation of predominantly Co₃O₄ spinel material. The remaining peaks in the 940-1100 cm⁻¹ area are attributed to surface hydroxyls arising from storage and handling under ambient conditions. Therefore, the structural information revealed by the FTIR spectra is consistent with the XPS data and confirms the change of chemical state of Co in the samples: the CoOOH in the CoO_x/Ni-Foam-150C was gradually transformed to CoO_x in the CoO_x/Ni-Foam-350C and CoO_x/Ni-Foam-500C samples upon annealing, and mostly became Co₃O₄ in CoO_x/Ni-Foam-650C sample.

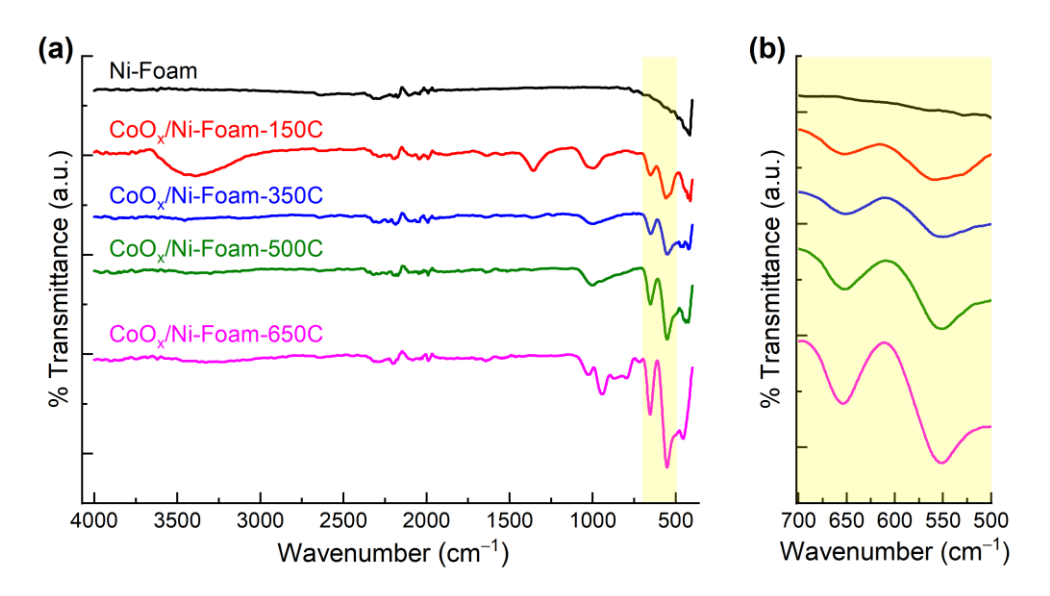


Figure 3. FTIR spectra of the Co-based samples supported on Ni foam. An expanded view of the highlighted region (500–700 cm⁻¹) in (a) is exhibited in (b).

The Co-based samples were subsequently tested and compared as electrocatalysts for the OER. LSV was first performed to evaluate the electrocatalytic performance for the OER. As shown in Figure 4a, the current density on all samples increased exponentially along with the increase of the overpotential, while the OER activity showed a substantial difference between the four samples, which deceased in the following order: CoO_x/Ni-Foam-150C > CoO_x/Ni-Foam-350C > CoO_x/Ni-Foam-650C. As the current densities in the LSV curves were normalized to the geometric surface area of each electrode, the different current densities might arise from the intrinsic activity as well as the ECSA, considering the change in the electrode morphology during the annealing at higher temperatures (Figure 1). There may be a concern about possibly exposed Ni surface that might participate in the OER catalysis. In our case, the long hydrothermal synthesis process typically leads to a full coating of the Ni foam by Co species, as shown by the SEM images. Moreover, the studies of Ni-based OER catalysts often show a Ni oxidation peak between 1.3 and 1.5 V vs RHE in the LSV or CV curves, ^{46–48} while the absence of such peak in all LSV curves of our samples can help confirm that Ni did not participate in the OER.

To compare their intrinsic activities for the OER, we quantified the ECSA of each electrode, which is proportional to its double-layer capacitance and can thus be measured by a CV method. As exhibited in Figure S8, CV scans were performed on each electrode at various scan rates in a potential window where only double-layer charging and discharging occur (no Faradaic process). The double-layer charging current was derived and then plotted vs the CV scan rate, and the slope of the linear regression gave the double-layer capacitance. As a result, the double-layer capacitance was determined for each electrode, which was further converted to ECSA using a conversion factor

of 40 μF cm⁻² in alkaline electrolyte.^{49,50} As expected, the ECSA was found to be the largest (~582 cm²) on the CoO_x/Ni-Foam-150C electrode, which decreased to ~427, 229, and 128 cm² for the CoO_x/Ni-Foam-350C, CoO_x/Ni-Foam-500C, and CoO_x/Ni-Foam-650C electrodes, respectively (Figure 4b). The ECSA data also confirmed the advantage of foam-based electrodes, which can provide high active surface areas to boost the electrocatalytic performance.⁵¹ The LSV curves were then normalized by their ECSA and the normalized current densities for the OER were derived, as shown in Figure 4c, which can reflect their difference in the intrinsic OER activities. Interestingly, the order of the intrinsic OER activity remained largely the same as that of the geometric current densities, with the highest OER activity on the CoO_x/Ni-Foam-150C electrode. It was noted that the ECSA-normalized activity was close between the CoO_x/Ni-Foam-500C and CoO_x/Ni-Foam-650C electrodes, while CoO_x/Ni-Foam-650C showed a slightly higher normalized activity, which is attributed to the higher Co³⁺ ratio of Co oxides in CoO_x/Ni-Foam-650C (Table 1).²⁶

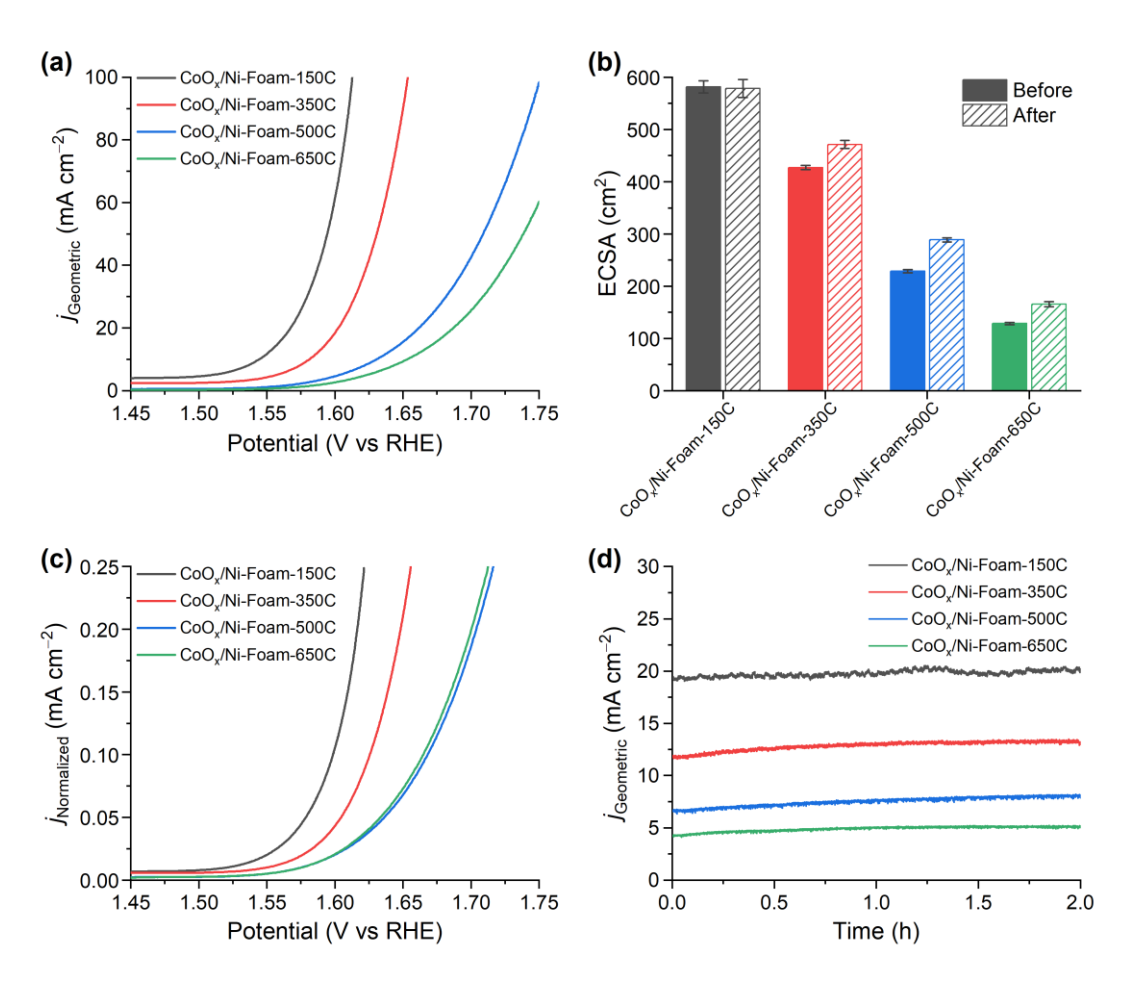


Figure 4. Electrocatalytic performance of the Co oxide samples supported on Ni foam for the OER. (a) LSV curves recorded on the different electrodes in 1 M KOH electrolyte. Scan rate = 10 mV s⁻¹. (b) ECSA measured on the electrodes before and after bulk electrolysis at 1.58 V vs RHE for 2 h. (c) ECSA-normalized current densities for the LSV curves measured on the electrodes in 1 M

KOH electrolyte. (d) Typical chronomperometric curves recorded for the bulk electrolysis of OER at 1.58 V vs RHE in 1 M KOH electrolyte.

In addition, bulk electrolysis was performed to further evaluate the OER on the electrodes at 1.58 V vs RHE in 1 M KOH electrolyte, with typical chronomperometric curves shown in Figure 4d. The bulk electrolysis data indicate a similar order of the OER activity between the electrodes. The current density remained largely stable or showed a slight increase in the 2-h bulk electrolysis, demonstrating a good stability of the electrodes. To further verify this, the ESCA of the electrodes was measured after 2-h bulk electrolysis and compared to those of the as-prepared electrodes. As shown in Figure 4b, the ECSA remained the same for the CoO_x/Ni-Foam-150C electrode after the electrolysis, while the ECSA increased slightly on the other three electrodes after 2-h electrolysis, which may be attributed to the oxidation and evolution of the electrodes during the electrolysis.^{27,31} To understand the structure-activity relationships, we further collected XPS spectra on the samples after 2-h electrolysis at 1.58 V vs RHE, as exhibited in Figure S9 and S10. Deconvolution of the Co 2p region of the samples gave multiple peaks at the same positions (Figure S9), with a higher ratio of Co³⁺ species than the corresponding as-prepared samples. The ratio of Co³⁺ species reached 79.7%, 75.8%, 69.8%, and 75.6% for the CoO_x/Ni-Foam-150C, CoO_x/Ni-Foam-350C, CoO_x/Ni-Foam-500C, and CoO_x/Ni-Foam-650C samples after 2-h electrolysis, respectively, as summarized in Table 1. This is attributed to the anodic oxidation conditions and may reflect the active state and phase of Co species during the OER.^{27,31} Interestingly, although the Co³⁺ ratio of CoO_x/Ni-Foam-150C increased after 2-h electrolysis, the ECSA remained the same (Figure 4b), which should be attributed to the transformation from Co(OH)2 to CoOOH that remained hexagonal shapes with little impact on the surface area.³¹ LSV curves were further collected on the electrodes after being tested for 2-h bulk electrolysis (Figure S11), where the OER activity on the CoO_x/Ni-Foam-150C electrode decreased a little bit, while the activities on the other three electrodes showed an increase after the 2-h test, consistent with the slight increase of current density in the bulk electrolysis test (Figure 4d). This should be correlated with the increase of Co³⁺ ratio in the samples after 2-h bulk electrolysis (Table 1), further confirming the more active Co³⁺ state for the OER. Overall, the order of their OER activities remained largely similar to that prior to electrolysis, indicating an intrinsic difference of their OER activities and a reasonable stability of the electrodes.

To look into the OER kinetics on the electrodes, Tafel slopes were derived from the LSV curves, which are 66, 71, 82, and 78 mV dec⁻¹ for the CoO_x/Ni-Foam-150C, CoO_x/Ni-Foam-350C, CoO_x/Ni-Foam-500C, and CoO_x/Ni-Foam-650C electrodes, respectively (Figure 5a). The Tafel slope increased monotonically from the CoO_x/Ni-Foam-150C to CoO_x/Ni-Foam-500C electrode, which agrees with the trend of their intrinsic OER activities (Figure 4c) and reveals a lower kinetic barrier for the OER on the electrodes prepared at a lower temperature, likely due to the different phases of Co oxyhydroxides or oxides. EIS spectra were also acquired on the electrodes at 1.58 V

vs RHE under typical OER conditions (Figure 5b). Fittings of the EIS spectra with a circuit model ¹⁴ (shown in the inset of Figure 5b) gave the impedance (energy barrier) for the electron transfer at the electrode-electrolyte interface, which also increased from CoO_x/Ni-Foam-150C to CoO_x/Ni-Foam-650C electrode, thus confirming the Tafel slope analysis. Therefore, both methods of analyzing the OER kinetics indicated the highest intrinsic activity and the lowest kinetic barrier for the OER on the CoO_x/Ni-Foam-150C electrode, which are attributed to the Co (oxy)hydroxide phases in the electrode that were confirmed by SEM images (hexagonal nanosheets morphology), XPS, and FTIR data. The Co (oxy)hydroxide phase or chemical state is most active for the OER and thus contributes significantly to the OER activity and dominates the OER kinetics.^{31,33} In contrast, other Co oxides derived at higher annealing temperatures cannot be oxidized or converted to the most active Co (oxy)hydroxide phase during the OER, although they may have similar ratios of high valence state (Co³⁺). Therefore, the design of OER catalysts should further increase or preserve such Co (oxy)hydroxide phase or chemical state in the electrodes.

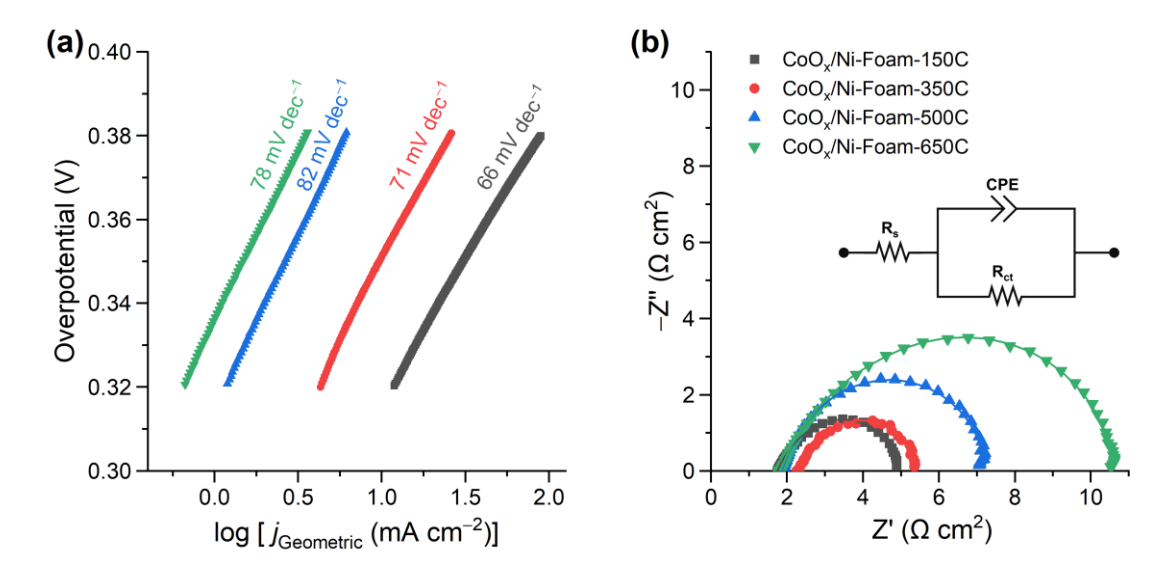


Figure 5. Kinetics of the OER on the Co-based electrodes. (a) Tafel slopes derived from the LSV curves. (b) Electrochemical impedance spectra acquired on the electrodes at 1.58 V vs RHE under OER conditions. Solid lines show the fittings of the EIS spectra using the circuit model in the inset, where R_s is the internal resistance, R_{ct} is the charge transfer resistance, and CPE is a constant phase element corresponding to electrical double layer pseudo-capacitance.¹⁴

CONCLUSIONS

In summary, we prepared and investigated Co (oxy)hydroxide or oxide nanosheets supported on Ni foam as electrocatalysts for the OER. The Co-based catalysts were fabricated by submerging a Ni foam support into a CoCl₂ solution, followed by heating to coat the support with Co species

and then annealing to various temperatures to convert the Co species to (oxy)hydroxides or oxides. The prepared $\text{CoO}_x/\text{Ni-foam}$ samples feature different morphologies and Co oxidation states and thus allow a comparison to reveal the effect of Co oxidation states on the OER. As a result, it was found that the electrode prepared with a lower annealing temperature exhibited a higher intrinsic activity for the OER than other electrodes prepared at higher temperatures, which was attributed to the presence of the Co (oxy)hydroxide species that are most active for the OER. These findings provide new insights into the structure-activity relationships as well as rational design of Co-based electrocatalysts for the OER towards efficient electrolyzers.

ASSOCIATED CONTENT

Supporting Information

The Supporting Information is available free of charge at ...

Additional materials characterization and electrochemical measurements (Figures S1–S11) (PDF)

AUTHOR INFORMATION

ORCID: Zackary S. Parsons: 0000-0001-7945-5128

Titel Jurca: 0000-0003-3656-912X Xiaofeng Feng: 0000-0002-9473-2848

Notes: The authors declare no competing financial interest.

ACKNOWLEDGMENTS

Z.S.P. and X.F. acknowledge the support of the National Science Foundation under Grant No. 1943732. Z.S.P. thanks the UCF College of Sciences and College of Graduate Studies for financial support. L.R.S. thanks the Ford Foundation Dissertation Fellowship for support. T.J. thanks the UCF Department of Chemistry, College of Sciences, and the Faculty Cluster Initiative for financial support. The authors also acknowledge the use of an XPS instrument supported by the NSF MRI: ECCS: 1726636.

REFERENCES

(1) Chu, S.; Majumdar, A. Opportunities and challenges for a sustainable energy future. *Nature* **2012**, *488*, 294–303.

- (2) O'Mullane, A. P.; Escudero-Escribano, M.; Stephens, I. E.; Krischer, K. The role of electrocatalysis in a sustainable future: From renewable energy conversion and storage to emerging reactions. *ChemPhysChem* **2019**, *20*, 2900–2903.
- (3) Roger, I.; Shipman, M. A.; Symes, M. D. Earth-abundant catalysts for electrochemical and photoelectrochemical water splitting. *Nat. Rev. Chem.* **2017**, *1*, 0003.
- (4) De Luna, P.; Hahn, C.; Higgins, D.; Jaffer, S. A.; Jaramillo, T. F.; Sargent, E. H. What would it take for renewably powered electrosynthesis to displace petrochemical processes? *Science* **2019**, *364*, eaav3506.
- (5) McCrory, C. C.; Jung, S.; Peters, J. C.; Jaramillo, T. F. Benchmarking heterogeneous electrocatalysts for the oxygen evolution reaction. *J. Am. Chem. Soc.* **2013**, *135*, 16977–16987.
- (6) Fabbri, E.; Habereder, A.; Waltar, K.; Kötz, R.; Schmidt, T. J. Developments and perspectives of oxide-based catalysts for the oxygen evolution reaction. *Catal. Sci. Technol.* **2014**, *4*, 3800–3821.
- (7) Frydendal, R.; Paoli, E. A.; Knudsen, B. P.; Wickman, B.; Malacrida, P.; Stephens, I. E.; Chorkendorff, I. Benchmarking the stability of oxygen evolution reaction catalysts: The importance of monitoring mass losses. *ChemElectroChem* **2014**, *1*, 2075–2081.
- (8) Hong, W. T.; Risch, M.; Stoerzinger, K. A.; Grimaud, A.; Suntivich, J.; Shao-Horn, Y. Toward the rational design of non-precious transition metal oxides for oxygen electrocatalysis. *Energy Environ. Sci.* **2015**, *8*, 1404–1427.
- (9) Song, J.; Wei, C.; Huang, Z. F.; Liu, C.; Zeng, L.; Wang, X.; Xu, Z. J. A review on fundamentals for designing oxygen evolution electrocatalysts. *Chem. Soc. Rev.* **2020**, *49*, 2196–2214.
- (10) Reier, T.; Oezaslan, M.; Strasser, P. Electrocatalytic oxygen evolution reaction (OER) on Ru, Ir, and Pt catalysts: A comparative study of nanoparticles and bulk materials. *ACS Catal.* **2012**, *2*, 1765–1772.
- (11) Browne, M. P.; Nolan, H.; Duesberg, G. S.; Colavita, P. E.; Lyons, M. E. Low-overpotential high-activity mixed manganese and ruthenium oxide electrocatalysts for oxygen evolution reaction in alkaline media. *ACS Catal.* **2016**, *6*, 2408–2415.
- (12) Wu, Z. Y.; Chen, F. Y.; Li, B.; Yu, S. W.; Finfrock, Y. Z.; Meira, D. M.; Yan, Q. Q.; Zhu, P.; Chen, M. X.; Song, T. W.; Yin, Z.; Liang, H. W.; Zhang, S.; Wang, G.; Wang, H. Non-iridium-based electrocatalyst for durable acidic oxygen evolution reaction in proton exchange membrane water electrolysis. *Nat. Mater.* **2023**, *22*, 100–108.

- (13) Burke, M. S.; Enman, L. J.; Batchellor, A. S.; Zou, S.; Boettcher, S. W. Oxygen evolution reaction electrocatalysis on transition metal oxides and (oxy)hydroxides: Activity trends and design principles. *Chem. Mater.* **2015**, *27*, 7549–7558.
- (14) Kou, T.; Wang, S.; Hauser, J. L.; Chen, M.; Oliver, S. R.; Ye, Y.; Guo, J.; Li, Y. Ni foam-supported Fe-doped β-Ni(OH)₂ nanosheets show ultralow overpotential for oxygen evolution reaction. *ACS Energy Lett.* **2019**, *4*, 622–628.
- (15) Batchellor, A. S.; Boettcher, S. W. Pulse-electrodeposited Ni–Fe (oxy)hydroxide oxygen evolution electrocatalysts with high geometric and intrinsic activities at large mass loadings. *ACS Catal.* **2015**, *5*, 6680–6689.
- (16) Burke, M. S.; Kast, M. G.; Trotochaud, L.; Smith, A. M.; Boettcher, S. W. Cobalt–iron (oxy)hydroxide oxygen evolution electrocatalysts: The role of structure and composition on activity, stability, and mechanism. *J. Am. Chem. Soc.* **2015**, *137*, 3638–3648.
- (17) Mabayoje, O.; Shoola, A.; Wygant, B. R.; Mullins, C. B. The role of anions in metal chalcogenide oxygen evolution catalysis: electrodeposited thin films of nickel sulfide as "pre-catalysts". *ACS Energy Lett.* **2016**, *I*, 195–201.
- (18) Sivanantham, A.; Ganesan, P.; Vinu, A.; Shanmugam, S. Surface activation and reconstruction of non-oxide-based catalysts through in situ electrochemical tuning for oxygen evolution reactions in alkaline media. *ACS Catal.* **2020**, *10*, 463–493.
- (19) Lei, C.; Lyu, S.; Si, J.; Yang, B.; Li, Z.; Lei, L.; Wen, Z.; Wu, G.; Hou, Y. Nanostructured carbon based heterogeneous electrocatalysts for oxygen evolution reaction in alkaline media. *ChemCatChem* **2019**, *11*, 5855–5874.
- (20) Wang, K.; Wang, X.; Li, Z.; Yang, B.; Ling, M.; Gao, X.; Lu, J.; Shi, Q.; Lei, L.; Wu, G.; Hou, Y. Designing 3d dual transition metal electrocatalysts for oxygen evolution reaction in alkaline electrolyte: Beyond oxides. *Nano Energy* **2020**, *77*, 105162.
- (21) Kang, W.; Wei, R.; Yin, H.; Li, D.; Chen, Z.; Huang, Q.; Zhang, P.; Jing, H.; Wang, X.; Li, C. Unraveling sequential oxidation kinetics and determining roles of multi-cobalt active sites on Co₃O₄ catalyst for water oxidation. *J. Am. Chem. Soc.* **2023**, *145*, 3470–3477.
- (22) Garcia-Mota, M.; Bajdich, M.; Viswanathan, V.; Vojvodic, A.; Bell, A. T.; Nørskov, J. K. Importance of correlation in determining electrocatalytic oxygen evolution activity on cobalt oxides. *J. Phys. Chem. C* **2012**, *116*, 21077–21082.
- (23) Bajdich, M.; García-Mota, M.; Vojvodic, A.; Nørskov, J. K.; Bell, A. T. Theoretical investigation of the activity of cobalt oxides for the electrochemical oxidation of water. *J. Am. Chem. Soc.* **2013**, *135*, 13521–13530.

- (24) Hutchings, G. S.; Zhang, Y.; Li, J.; Yonemoto, B. T.; Zhou, X.; Zhu, K.; Jiao, F. In situ formation of cobalt oxide nanocubanes as efficient oxygen evolution catalysts. *J. Am. Chem. Soc.* **2015**, *137*, 4223–4229.
- (25) Du, J.; Li, C.; Wang, X.; Shi, X.; Liang, H. P. Mesoporous ultrathin cobalt oxides nanosheets grown on carbon cloth as a high-performance electrode for oxygen evolution reaction. *ACS Appl. Energy Mater.* **2019**, *2*, 1977–1987.
- (26) Haase, F. T.; Bergmann, A.; Jones, T. E.; Timoshenko, J.; Herzog, A.; Jeon, H. S.; Rettenmaier, C.; Cuenya, B. R. Size effects and active state formation of cobalt oxide nanoparticles during the oxygen evolution reaction. *Nat. Energy* **2022**, *7*, 765–773.
- (27) Gu, W.; Hu, L.; Zhu, X.; Shang, C.; Li, J.; Wang, E. Rapid synthesis of Co₃O₄ nanosheet arrays on Ni foam by in situ electrochemical oxidization of air-plasma engraved Co(OH)₂ for efficient oxygen evolution. *Chem. Commun.* **2018**, *54*, 12698–12701.
- (28) Liu, Z.; Xiao, Z.; Luo, G.; Chen, R.; Dong, C. L.; Chen, X.; Cen, J.; Yang, H.; Wang, Y.; Su, D.; Li, Y.; Wang, S. Defects-induced in-plane heterophase in cobalt oxide nanosheets for oxygen evolution reaction. *Small* **2019**, *15*, 1904903.
- (29) Li, L.; Hu, Z.; Tao, L.; Xu, J.; Yu, J. C. Efficient electronic transport in partially disordered Co₃O₄ nanosheets for electrocatalytic oxygen evolution reaction. *ACS Appl. Energy Mater.* **2020**, *3*, 3071–3081.
- (30) Bergmann, A.; Jones, T. E.; Moreno, E. M.; Teschner, D.; Chernev, P.; Gliech, M.; Reier, T.; Dau, H.; Strasser, P. Unified structural motifs of the catalytically active state of Co(oxyhydr)oxides during the electrochemical oxygen evolution reaction. *Nat. Catal.* **2018**, *1*, 711–719.
- (31) Mefford, J. T.; Akbashev, A. R.; Kang, M.; Bentley, C. L.; Gent, W. E.; Deng, H. D.; Alsem, D. H.; Yu, Y. S.; Salmon, N. J.; Shapiro, D. A.; Unwin, P. R.; Chueh, W. C. Correlative operando microscopy of oxygen evolution electrocatalysts. *Nature* **2021**, *593*, 67–73.
- (32) Moysiadou, A.; Lee, S.; Hsu, C. S.; Chen, H. M.; Hu, X. Mechanism of oxygen evolution catalyzed by cobalt oxyhydroxide: Cobalt superoxide species as a key intermediate and dioxygen release as a rate-determining step. *J. Am. Chem. Soc.* **2020**, *142*, 11901–11914.
- (33) Luan, C.; Corva, M.; Hagemann, U.; Wang, H.; Heidelmann, M.; Tschulik, K.; Li, T. Atomic-scale insights into morphological, structural, and compositional evolution of CoOOH during oxygen evolution reaction. *ACS Catal.* **2023**, *13*, 1400–1411.
- (34) Hu, Y.; Hu, C.; Du, A.; Xiao, T.; Yu, L.; Yang, C.; Xie, W. Interfacial evolution on Cobased oxygen evolution reaction electrocatalysts probed by using *in situ* surface-enhanced Raman spectroscopy. *Anal. Chem.* **2023**, *95*, 1703–1709.

- (35) Huang, J.; Sheng, H.; Ross, R. D.; Han, J.; Wang, X.; Song, B.; Jin, S. Modifying redox properties and local bonding of Co₃O₄ by CeO₂ enhances oxygen evolution catalysis in acid. *Nat. Commun.* **2021**, *12*, 3036.
- (36) Liu, C.; Qian, J.; Ye, Y.; Zhou, H.; Sun, C. J.; Sheehan, C.; Zhang, Z.; Wan, G.; Liu, Y. S.; Guo, J.; Li, S.; Shin, H.; Hwang, S.; Gunnoe, T. B.; Goddard, W. A.; Zhang, S. Oxygen evolution reaction over catalytic single-site Co in a well-defined brookite TiO₂ nanorod surface. *Nat. Catal.* **2021**, *4*, 36–45.
- (37) Zhang, H.; Zhou, W.; Dong, J.; Lu, X. F.; Lou, X. W. Intramolecular electronic coupling in porous iron cobalt (oxy)phosphide nanoboxes enhances the electrocatalytic activity for oxygen evolution. *Energy Environ. Sci.* **2019**, *12*, 3348–3355.
- (38) Pei, Z.; Lu, X. F.; Zhang, H.; Li, Y.; Luan, D.; Lou, X. W. Highly efficient electrocatalytic oxygen evolution over atomically dispersed synergistic Ni/Co dual sites. *Angew. Chem. Int. Ed.* **2022**, *61*, e202207537.
- (39) Lu, M.; Zheng, Y.; Hu, Y.; Huang, B.; Ji, D.; Sun, M.; Li, J.; Peng, Y.; Si, R.; Xi, P.; Yan, C. H. Artificially steering electrocatalytic oxygen evolution reaction mechanism by regulating oxygen defect contents in perovskites. *Sci. Adv.* **2022**, *8*, eabq3563.
- (40) Yang, J.; Liu, H.; Martens, W. N.; Frost, R. L. Synthesis and characterization of cobalt hydroxide, cobalt oxyhydroxide, and cobalt oxide nanodiscs. *J. Phys. Chem. C* **2010**, *114*, 111–119.
- (41) McIntyre, N. S.; Cook, M. G. X-ray photoelectron studies on some oxides and hydroxides of cobalt, nickel, and copper. *Anal. Chem.* **1975**, *47*, 2208–2213.
- (42) Han, Y.; Axnanda, S.; Crumlin, E. J.; Chang, R.; Mao, B.; Hussain, Z.; Ross, P. N.; Li, Y.; Liu, Z. Observing the electrochemical oxidation of Co metal at the solid/liquid interface using ambient pressure X-ray photoelectron spectroscopy. *J. Phys. Chem. B* **2018**, *122*, 666–671.
- (43) He, T.; Chen, D.; Jiao, X.; Wang, Y. Co₃O₄ nanoboxes: surfactant-templated fabrication and microstructure characterization. *Adv. Mater.* **2006**, *18*, 1078–1082.
- (44) Pandey, B. K.; Shahi, A. K.; Gopal, R., 2015. Magnetic colloid by PLA: Optical, magnetic and thermal transport properties. *Appl. Surf. Sci.* **2015**, *347*, 461–470.
- (45) Alburquenque, D.; Vargas, E.; Denardin, J. C.; Escrig, J.; Marco, J. F.; Ortiz, J.; Gautier, J. L. Physical and electrochemical study of cobalt oxide nano-and microparticles. *Mater. Charact.* **2014**, *93*, 191–197.
- (46) Ali Akbari, M. S.; Bagheri, R.; Song, Z.; Najafpour, M. M. Oxygen-evolution reaction by nickel/nickel oxide interface in the presence of ferrate(VI). *Sci. Rep.* **2020**, *10*, 8757.

- (47) Cheng, W.; Xi, S.; Wu, Z. P.; Luan, D.; Lou, X. W. In situ activation of Br-confined Ni-based metal-organic framework hollow prisms toward efficient electrochemical oxygen evolution. *Sci. Adv.* **2021**, *7*, eabk0919.
- (48) Hua, W.; Sun, H.; Jiang, M.; Ren, L.; Zhang, Y.; Wang, J. G. Cascading reconstruction to induce highly disordered Fe–Ni(O)OH toward enhanced oxygen evolution reaction. *J. Mater. Chem. A* **2022**, *10*, 7366–7372.
- (49) Yoo, J.; Byun, S.; Lee, C. W.; Yoo, C. Y.; Yu, J. Precisely geometry controlled microsupercapacitors for ultrahigh areal capacitance, volumetric capacitance, and energy density. *Chem. Mater.* **2018**, *30*, 3979–3990.
- (50) Conway, B. E.; Pell, W. G. Double-layer and pseudocapacitance types of electrochemical capacitors and their applications to the development of hybrid devices. *J. Solid State Electrochem.* **2003**, *7*, 637–644.
- (51) Zheng, W.; Liu, M.; Lee, L. Y. S. Best practices in using foam-type electrodes for electrocatalytic performance benchmark. *ACS Energy Lett.* **2020**, *5*, 3260–3264.

Table of Contents (TOC) Graphic:

